

# The effect of detector nonlinearity on WFIRST PSF profiles for weak gravitational lensing measurements

A. A. Plazas<sup>†a</sup>, C. Shapiro<sup>a,b</sup>, A. Kannawadi<sup>c</sup>, R. Mandelbaum<sup>c</sup>, J. Rhodes<sup>a,b,d</sup>, & R. Smith<sup>b</sup>

<sup>†</sup>Andres.A.Plazas.Malagon@jpl.nasa.gov

<sup>a</sup>*Jet Propulsion Laboratory, California Institute of Technology, 4800 Oak Grove Dr., Pasadena, CA 91109, USA*

<sup>b</sup>*California Institute of Technology, 1200 E. California Blvd., CA 91125, USA*

<sup>c</sup>*McWilliams Center for Cosmology, Department of Physics, Carnegie Mellon University, Pittsburgh, PA 15213, USA*

<sup>d</sup>*Institute for the Physics and Mathematics of the Universe, 5-1-5 Kashiwanoha, Kashiwa, Chiba Prefecture 277-8583, Japan*

## ABSTRACT

Weak gravitational lensing (WL) is one of the most powerful techniques to learn about the dark sector of the universe. To extract the WL signal from astronomical observations, galaxy shapes must be measured and corrected for the point spread function (PSF) of the imaging system with extreme accuracy. Future WL missions – such as NASA’s Wide-Field Infrared Survey Telescope (WFIRST) – will use a family of hybrid near-infrared CMOS detectors (HAWAII-4RG) that are untested for accurate WL measurements. Like all image sensors, these devices are subject to conversion gain nonlinearities (voltage response to collected photo-charge) that bias the shape and size of bright objects such as reference stars that are used in PSF determination. We study this type of detector nonlinearity (NL) and show how to derive requirements on it from WFIRST PSF size and ellipticity requirements. We simulate the PSF optical profiles expected for WFIRST and measure the fractional error in the PSF size ( $\Delta R/R$ ) and the absolute error in the PSF ellipticity ( $\Delta e$ ) as a function of star magnitude and the NL model. For our nominal NL model (a quadratic correction), we find that, uncalibrated, NL can induce an error of  $\Delta R/R = 0.01$  and  $\Delta e_2 = 1.75 \times 10^{-3}$  in the H158 band-pass for the brightest unsaturated stars in WFIRST. In addition, our simulations show that to limit the bias of  $\Delta R/R$  and  $\Delta e$  in the H158 band to  $\sim 10\%$  of the estimated WFIRST error budget, the quadratic NL parameter  $\beta$  must be calibrated to  $\sim 1\%$  and  $\sim 2.4\%$ , respectively. We present a fitting formula that can be used to estimate WFIRST detector NL requirements once a true PSF error budget is established.

## 1. Introduction

Weak gravitational lensing (WL) has been identified as a powerful probe of the nature and evolution of the components of the Universe. In particular, *cosmic shear*—the subtle distortions of background galaxy shapes by the large-scale structure of the Universe—constrains the properties of dark matter and dark energy through the measurement of the expansion history and growth of structure of the Universe (Réfrégier 2003; Hoekstra and Jain 2008; Kilbinger 2015). WL measurements also allow to test the validity of General Relativity that relates the gravitational potential to the matter-energy distribution. Several surveys in the visible part of the spectrum of  $> 1000 \text{ deg}^2$  of the sky are currently underway and use the WL signal from hundreds of millions of galaxies as one of their central scientific techniques (*e.g.*, the Dark Energy Survey (DES), Diehl and Dark Energy Survey Collaboration 2012, Jarvis et al. 2015; the Kilo-Degree Survey (KiDS), Kuijken et al. 2015; and the Hyper Suprime-Cam Survey (HSC), Miyazaki et al. 2012). In addition, future ground- and space-based surveys and missions in the visible and near infra-red (NIR) are planned to image more than  $O(10^9)$  galaxies in the next decade (*e.g.*, the Large Synoptic Survey Telescope (LSST), Ivezić et al. 2008; the Euclid spacecraft, Laureijs et al. 2011; and NASA’s Wide-Field Infrared Survey Telescope (WFIRST), Green et al. 2012, Spergel et al. 2013, Spergel et al. 2015).

The process of extracting the WL signal from images of the sky, in the presence of intrinsic galaxy ellipticity variations that are  $\sim 0.4$  r.m.s, is highly non-trivial. It must be done through a statistical analysis of large galaxy samples, with a careful control of systematic uncertainties. The dominant signal produced by WL can be described by a local linear transformation of the source image that produces a shear (a complex, spin-2 field of components  $\gamma_1$  and  $\gamma_2$ ) and a scalar magnification, both of which have an r.m.s. amplitude of only  $\sim 2\%$  in the case of cosmic shear. Most of the background galaxies usable by WL are at high redshift (with low signal-to-noise (S/N) ratio) and with a size comparable or smaller than the Point Spread Function (PSF) of the imaging system. Incorrect estimation of the size of the PSF induces a modulation in the signal (multiplicative errors), and errors in the estimation of the PSF ellipticity propagate into asymmetries that produce coherent spurious patterns (additive errors) that mimic the WL signal. Bright stars are commonly used to estimate the PSF, and then this information must be interpolated to the observed galaxy positions to deconvolve the PSF contribution and measure the galaxy shape (in the form of a complex ellipticity  $e = e_1 + ie_2$ ) to estimate the shear field.<sup>1</sup> This interpolation step introduces systematic errors if the information inferred from the stars does not fully constrain the PSF at the galaxy position with the required accuracy. In order not to bias the determination of dark energy and other cosmological parameters in Stage IV surveys (in the language of Albrecht et al. 2006), the ellipticity and relative size of the PSF must be known to an accuracy of  $O(10^{-3})$  (Huterer et al.

---

<sup>1</sup>Most of the shape measurement algorithms to date rely on the accurate measurements of galaxy shapes to produce an estimator of the WL shear field ( $\gamma_1, \gamma_2$ ). However, recent algorithms propose skipping this step and creating a direct shear estimator through Bayesian analysis (Bernstein and Armstrong 2014, Bernstein et al. 2015, Schneider et al. 2015).

2006, Amara and Réfrégier 2008, Paulin-Henriksson et al. 2008, Paulin-Henriksson et al. 2009, Massey et al. 2013, Cropper et al. 2013) or better ( $4.7 \times 10^{-4}$  for the knowledge of the WFIRST PSF ellipticity, Spergel et al. 2013).

Systematic errors that originate from a telescope’s detectors (image sensors) introduce biases in astronomical observables such as photometry and astrometry that propagate into shear measurement biases. These type of errors have been extensively studied in the case of thick, fully-depleted, high-resistivity Charge Coupled-Devices (CCDs), which are the detectors of choice for many current and planned surveys such as DES, HSC, and LSST (Stubbs 2014, Plazas et al. 2014, Gruen et al. 2015). It is of great importance to quantify the impact of these sensor effects on the inference of cosmological parameters, in particular through WL (Jarvis 2014, Mandelbaum 2015, Meyers and Burchat 2014). Future missions such as the James Webb Space Telescope and WFIRST will utilize a family of near-infrared detectors that are also subject to effects such as nonlinearity, reciprocity failure (Bohlin et al. 2005, Biesiadzinski et al. 2011), interpixel capacitance (IPC) (McCullough 2008, Kannawadi et al. 2015), and persistence (Smith et al. 2008). These effects can imprint biases on weak lensing shape measurements if not taken into account.

In this paper we study the effect of nonlinear detector conversion gain (voltage response to collected photo-charge) on PSF size and ellipticity in the context of the NIR detectors that will be used by NASA’s WFIRST mission. This type of detector nonlinearity (NL) will tend to attenuate the measured flux in bright stars and broadening the inferred PSF. In other words, NL preferentially depresses the flux in the core of the PSF relative to the wings, thus complicating its deconvolution from the observed galaxy image, which itself is fainter and less subject to the effects of NL. In addition, even though NL does not induce a spurious ellipticity by itself, it modifies the PSF ellipticity if the PSF is anisotropic. Our analysis is also useful to set preliminary requirements on NL for these sensors. Once characterized, NL can be corrected in each image, and remaining residuals will depend on the accuracy in the knowledge of the NL parameters and their spatial variation. We use the `python/C++` code `GalSim`<sup>2</sup> (Rowe et al. 2015) to simulate WFIRST PSF profiles and to analyze the impact of NL on PSF size and ellipticity.

In Section 2 we summarize the main characteristics of the NIR detectors that will be used in WFIRST and describe NL. In Section 3 we describe the simulations we create to study NL for WFIRST PSF profiles. Section 4 presents our main results on fractional errors in size and absolute errors in ellipticity caused by NL, as function of relevant parameters such as the model parameters and PSF magnitude. We also study the effect of the spatial variability of the NL model across the pixel array. We conclude in Section 5 with a discussion of our results and how they can be used in the derivation of NIR detector specifications to satisfy WL accuracy requirements.

---

<sup>2</sup><https://github.com/GalSim-developers>, <https://wfirst.ipac.caltech.edu/sims/Code.html>

## 2. Voltage nonlinearity in the NIR detectors of WFIRST

The WFIRST mission will use a 2.4 m telescope equipped with a Wide Field Instrument (WFI) with 6 bandpass filters: Z087, Y106, J129, W149, H158, and F184 (Spergel et al. 2015).<sup>3</sup> The WFI will perform a high-latitude survey (HLS), imaging over an area of 2200 deg<sup>2</sup> in four NIR ( $\sim 0.92\text{--}2.00\ \mu\text{m}$ ) bands (Y106, J129, H158, and F184) down to a  $5\sigma$  point-source AB magnitude of 26.7 in the J129 band. The weak lensing program in the HLS will measure shapes of about 380 million galaxies in the J129, H158, and F184 bands (Spergel et al. 2015).

The WFI possesses a wide-field channel that has a Focal Plane Assembly (FPA) of  $18\ 4k \times 4k$  HgCdTe (mercury, cadmium, and telluride) NIR detectors, arranged in a  $6 \times 3$  layout and with a pixel size and scale of  $10\ \mu\text{m}$  and  $0.11$  arcseconds per pixel, respectively. The HgCdTe NIR detectors are manufactured by Teledyne Imaging Systems, and are part of a family of detectors known as Hawaii-XRG (HXRG), where X denotes the detector width in thousands of pixels<sup>4</sup>.

The detector arrays are fabricated with a hybrid complementary metal-oxide-semiconductor (CMOS) architecture, which combines the qualities of HgCdTe to detect infra-red light (*e.g.*, altering the relative molar contributions of mercury and cadmium allows one to tune the band gap up to an order of magnitude) and the advanced readout performance of integrated circuits. Light is absorbed, converted to charge through the photoelectric effect, and collected by electric fields generated by a reverse-biased p-n junction in the detector layer. The charge per pixel is then converted to a voltage and amplified through a source follower. This operation is performed in the silicon readout integrated circuit (ROIC) layer, which is connected to the HgCdTe detection layer by indium interconnects (one indium bump per pixel). Finally, the ROIC transfers the signal (and for this it is also known as “multiplexer”) to the off-chip electronics at the edge of the FPA, where it is digitized through analog-to-digital converters (Beletic et al. 2008).

An ideal detector would produce a measurable signal that is proportional to the detected photons. However, there are several places in the signal chain where this expected linearity is not realized, and the conversion of charge to measured voltage (or digital numbers) becomes nonlinear. Each pixel’s p-n junction acts as a parallel-plate capacitor, and as charge accumulates the depletion region narrows, causing a deviation from linearity of the charge-to-voltage conversion relation. Nonlinearity can also be introduced through the electronic gain of the ROIC. Furthermore, the charge accumulation rate might be a function of the photon-accumulation rate, an effect known as count-rate nonlinearity or reciprocity failure (RF) (Smith et al. 2008, Biesiadzinski et al. 2011). The first two types of nonlinearity depend only on fluence (integrated signal) as opposed to RF, which is flux dependent. They can be analyzed together in a single transfer function typically called “nonlinearity” (NL). We study the impacts of NL (more relevant at high signals) on PSF

---

<sup>3</sup>In addition to a integral field unit and a coronagraph for supernovae and exoplanet studies, respectively.

<sup>4</sup>HAWAII stands for HgCdTe Astronomical Wide Area Infrared Imager, and RG stands for “Reference pixels and Guide mode”.

116 measurements in this paper, while we leave investigations on the consequences of RF (relevant at  
117 lower signals) on WL measurements for future work.

Assuming that the dominant contribution to nonlinearity is the varying capacitance of the pixel p-n junction, the correction to the detector signal is well approximated by a quadratic term:

$$S(Q) = Q - \beta Q^2 \quad (1)$$

118 Here,  $Q$  is the true number of elementary charges collected in the pixel,  $S$  is the number inferred  
119 from the voltage change at the sense node, and  $\beta$  is a constant. To estimate  $\beta$ , we compute  
120  $Q(V) = C(V) * V/q_e$ , where  $q_e$  is the elementary charge, and the total capacitance is given by  
121 the varying junction capacitance plus a constant  $C(V) = C_{\text{jn}}(V) + C_{\text{fix}}$ . The junction capacitance  
122 varies as (McCaughrean 1987)

$$C_{\text{jn}}(V) \propto (1 + V/V_{\text{bi}})^{-1/2}. \quad (2)$$

123 Here,  $V_{\text{bi}}$  is the “built in” potential of the junction and  $V = V_{\text{DSUB}} - V_{\text{RESET}} + \delta V$ , where  $V_{\text{DSUB}}$   
124 is the constant potential at the diode cathode,  $V_{\text{RESET}}$  is the initial potential at the anode, and  
125  $\delta V$  is the change in anode potential due to accumulated photocharge. As an example, we plug in  
126 measurements of a  $2.4\mu\text{m}$  cutoff H2RG by Finger 2006:<sup>5</sup>

$$\begin{aligned} V_{\text{bi}} &= 0.412 \text{ V} \\ V_{\text{DSUB}} &= 1 \text{ V} \\ V_{\text{RESET}} &= 0.5 \text{ V} \\ C_{\text{fix}} &= 17.8 \text{ fF} \\ C_{\text{jn}}(V = .912 \text{ V}) &= 30 \text{ fF} \end{aligned}$$

127 Using these parameters to compute  $Q(V)$  for  $0 \leq \delta V \leq 0.3 \text{ V}$  (corresponding to maximum  
128  $Q=60115$ ) and then inverting to find  $S(Q)$ , we find it is well-fit (to 0.1% or better) by Eqn. 1  
129 with  $\beta = 1.18 \times 10^{-6}$ . In practice, HXRG calibrations have included additional polynomial param-  
130 eters which can reduce residuals, extend the range of valid  $Q$ , and account for additional nonlinear  
131 effects (Hilbert 2004, Hilbert 2008, Hilbert 2014); however, the additional parameters are highly  
132 degenerate, resulting in large variances in the fitted values. For our purposes, it suffices to analyze  
133 the shape-distorting effects of nonlinearity using a single parameter,  $\beta$ , which encapsulates most of  
134 the effect. In this paper we chose a nominal value of  $\beta_0 = 5 \times 10^{-7}$ , which is near the midpoint of  
135 the measured range for  $\beta$  in Hilbert 2014.

136 To illustrate the effect of NL on photometry, consider nearly saturated stars in the HLS. Using  
137 PSF profiles with a simulated AB magnitude up to 18.3 for an exposure time of 168.1 seconds  
138 (expected for the HLS), the total flux in each band is shown in Table 1, along with the peak  
139 pixel value. When the profile is drawn on a pixelated postage stamp with a scale of  $p = 0.11$

---

<sup>5</sup><https://www.eso.org/sci/meetings/2006/neon-2006/Finger.pdf>

arcseconds and placed on the center of the pixel<sup>6</sup>, this particular magnitude produces a peak charge of  $\sim 1 \times 10^5 \text{ e}^-$  (Y106 band, see Table 1), which represents about 90% of the typical pixel full well value of  $1.1 \times 10^5 \text{ e}^-$ .<sup>7</sup> At this level of charge, the signal attenuation due to NL for the nominal  $\beta_0$  value is of about 5% (Eqn. 1).

Calculations with the **Trilegal** galaxy model<sup>8</sup> (Girardi et al. 2012) show that there will be approximately 20 stars at or brighter than this magnitude (18.3) and flux level per detector.<sup>9</sup> We assume that galaxies will have about two orders of magnitude fewer total electrons than bright stars, and therefore for this quadratic model, star shapes are distorted by NL and galaxies are (approximately) not, which would result in an incorrect PSF correction if not accurately calibrated. Thus our goal is apply NL to simulated WFIRST PSF profiles and quantify the impact on PSF properties such as size and shape.

### 3. Methods

#### 3.1. Simulations

We use the publicly available **GalSim** code (v1.3) to simulate the impact of NL on the WFIRST PSF shape and size. **GalSim** is a **python/C++** open-source code that allows the user to create simulations of astronomical objects, and it was developed by the weak lensing community to investigate shape measurement algorithms and systematics.

Kannawadi et al. (2015) have developed within **GalSim** v1.3 a WFIRST module called “**galsim.wfirst**”, which allows the simulation of a PSF profile according to the optical design characteristics of the WFIRST WFI (Pasquale et al. 2014)<sup>10</sup> through the calling of the **galsim.wfirst.getPSF** routine. This routine returns a **python** dictionary indexed by each one of the 18 H4RG detectors of the FPA. It uses the optical configuration of the pupil plane<sup>11</sup> to simulate PSF images in any

---

<sup>6</sup>Note that the peak value is a function of the PSF profile centroid location within the pixel, as well as pixel resolution. When drawing the PSF profiles in our simulations, we randomize the PSF centroid within the native scale pixel, as described in Section 3.

<sup>7</sup>Dave Content, private communication.

<sup>8</sup><http://stev.oapd.inaf.it/cgi-bin/trilegal>

<sup>9</sup>We thank Christopher Hirata, who performed these calculations. The NIR filter sets used in **Trilegal** had to be converted from the vega to the AB magnitude system. The code was run at the South Galactic Pole with the SDSS and 2MASS (*ugriz* and *JHK<sub>s</sub>*) filters in  $1 \text{ deg}^2$  and interpolated to WFIRST filter centers, which ignores the fact that stars have spectral structure in the NIR, but gives a result good to about 10%. The number of stars quoted in the text is expected to be higher at moderate galactic latitudes.

<sup>10</sup>Pasquale et al. 2014 discuss the so-called “Cycle 4” optical design, whereas the **GalSim** WFIRST module—used in this work—uses files corresponding to “Cycle 5”.

<sup>11</sup>The pupil plane configuration is not circular in all the bands but the simulated PSFs use circular apertures.

WFIRST WFI bandpass filter, with expected optical aberrations approximated as a linear combination of Zernike polynomials (up to Noll order equal to 11, Noll 1976). For this work, we have created simulations in the four bands of the HLS. A central circular obscuration (30%) and six support struts are included as well. The pupil plane configurations and Zernike models are publicly available.<sup>12</sup>

The current version of the module does not include PSF variations across the detector field of view, and the PSF returned corresponds to that at each detector center. In addition, the module assumes that the pupil plane configuration of all the six bands is the same and equivalent to that of the “red” bands (*i.e.*, W149, H158, and F184), and that the struts are not, in general, radial nor evenly spaced. The module generates PSF models that do not include pointing jitter nor charge diffusion. These effects could be added to the profile (*e.g.*, by means of an extra convolution with a Gaussian profile in the case of diffusion), but we did not include them in our simulations. Their effect would be to create a slightly larger PSF, reducing the impact NL. Their omission makes our results slightly conservative.

The ellipticity of the WFI PSF varies over the field of view due to optical aberrations. To make our results conservative, we simulate only detector #18, whose PSF was determined to have the largest ellipticity (see §3.2 for a description of the shape measurement method used) across all bands among all the detectors (Table 1). We also evaluate the PSF at the mean wavelength weighted by each bandpass or effective wavelength, resulting in an (achromatic) `galsim.OpticalPSF` object. We then form an effective PSF by convolving the profile with a 2D top-hat profile of length equal to the nominal angular scale of the WFIRST WFI (`galsim.wfirst.pixel_scale= 0.11` arcseconds per pixel).

The WFI PSF is undersampled by design. In order to maximize the field of view, detectors in instruments of space missions are usually built with a physical size that results in undersampled images, which fail to satisfy the Nyquist-Shannon criterium for the maximum band limit set by the optical response of the system, and therefore produce aliased images.<sup>13</sup> In general, it is not possible to recover all the information of a continuous function from a discrete sample of points if the image is aliased, and measurements of astronomical object’s properties such as magnitude and shape will be erroneous (Lauer 1999a, Fruchter 2011, Rhodes et al. 2007). Also, in particular, we found that our shape measurement algorithm fails when most light is concentrated in a few pixels.

To overcome this problem in real data, multiple dithered exposures are taken, and then processed by an image combination algorithm (Lauer 1999b, Fruchter and Hook 2002, Bertin 2006, Rowe et al. 2011) in order to produce an oversampled image that satisfies the Nyquist-Shannon criterium. To study NL with simulations, however, we do not need to make use of such external

---

<sup>12</sup>[http://wfirst.gsfc.nasa.gov/science/sdt\\_public/wps/references/instrument/](http://wfirst.gsfc.nasa.gov/science/sdt_public/wps/references/instrument/)

<sup>13</sup>The Nyquist-Shannon criterium states that the sampling interval  $p$  must satisfy  $p < 1/(2u_{max})$ , where  $u_{max}$  is the highest frequency in the signal, in order to avoid aliasing.

Band	Min. $\lambda$ ( $\mu\text{m}$ )	Max. $\lambda$ ( $\mu\text{m}$ )	$\lambda_{\text{eff}}$ ( $\mu\text{m}$ )	$b(\lambda)$ ( $\times 10^5$ ) ( $\text{e}^-$ )	peak value ( $\times 10^5$ ) ( $\text{e}^-$ )	$e_1$ (#18)	$e_2$ (#18)	$\sigma$ (pix) (#18)
Y106	0.900	1.230	1.061	2.7621	1.00237	-0.0163	0.2035	1.7020
J129	1.095	1.500	1.292	2.8267	0.89742	-0.0127	0.1325	1.717
H158	1.340	1.830	1.577	2.7922	0.38654	-0.0089	0.0802	1.832
F184	1.630	2.060	1.837	1.8346	0.71890	-0.0071	0.0550	1.995

Table 1: The first column lists the four bands that will be used in the HLS. For weak lensing analysis, multi-band shape measurement will be done in bands J129, H158, and F184. Columns 2, 3, and 4 show their minimum, maximum, and effective wavelengths, respectively (from Kannawadi et al. 2015). Column 5 shows the baseline total flux (in electrons)  $b(\lambda)$  of Eq. 4 at AB magnitude 18.3 (at 161.1 seconds of exposure time) in each band as calculated in `GalSim`, while column 6 shows the peak value for each profile rendered at the native pixel scale ( $p = 0.11$  arcseconds per pixel) at that same magnitude. The last three columns show the ellipticity components and size of the WFIRST PSF profile (drawn at a resolution of  $p/N$ , with  $N = 3$ ) in detector number 18 as calculated by the adaptive moments routine in `GalSim`. Chip #18 was found to possess the largest values of absolute PSF ellipticity.

software—which can be computationally expensive—to produce an image at higher resolution. Instead, we render the convolved PSF profile—including the pixel response at its native scale—as a `GalSim` object at a high resolution through the method `galsim.GSObject.drawImage`,<sup>14</sup> setting the parameter `scale` to  $p/N$ , where  $N$  is a positive integer and  $p$  is the native pixel scale.

Defining  $Q \equiv 1/p \times u_{\text{max}}$  as the sampling factor ( $Q < 2$ ,  $Q = 2$ , and  $Q \geq 2$  represent under-, critically, and over-sampled images, respectively), we see that in order to produce an over-sampled image ( $Q \geq 2$ ), the Nyquist-Shannon criterium implies that  $N$  must be given by (see *e.g.*, Marks 2009, Shapiro et al. 2013)

$$N = \frac{2p}{\lambda_{\text{min}} F} \quad (3)$$

where  $p$  is the pixel size,  $\lambda_{\text{min}}$  is the shortest wavelength in a given filter, and  $F$  is the the f-number of the telescope. In the case of the WFIRST telescope,  $p = 10 \mu\text{m}$  and  $F = 7.8$ , resulting in  $N \geq 3$  ( $N \geq 2$ ) for the J129 (H158) band. Thus, we have chosen to set  $N = 3$  in our simulations to ensure oversampling. At this resolution, it will also be possible to study the impact of centroid shifts within the native pixels (since NL depends on the absolute pixel values it will also depend on where the star is centered within a particular pixel), and therefore for our simulations we randomly vary the PSF centroid within a native pixel. **[WHAT DOES THIS MEAN?]**

<sup>14</sup>The keyword `method` should be set to “`no_pixel`” when calling `galsim.GSObject.drawImage`, since by default it convolves its argument profile with a boxcar of length `pixel_scale`. This extra convolution must be turned off because the effective PSF profile we create already includes this pixel response.



Notice that this method to approximate oversampled images can only be used in the case of sensor effects such as NL, which only depend on each pixel individually. In the case of other effects that correlate the signal in one pixel with the signal of its neighbors (such as IPC), the effect should be applied to the native scale of the detector and then a properly sampled image should be generated through adequate combination of several dithered images before performing any analysis (see for instance the “interleaving” algorithm of Kannawadi et al. 2015, also included in `GalSim`).

The PSF profiles are drawn into squared postage stamps of size  $1.5k$  pixels ( $k = 64$ ), large enough to ensure that most ( $\sim 96\%$ ) of the total PSF flux is contained in the stamp. Each profile object was assigned a total flux of

$$f = b(\lambda) \times 10^{0.4(18.3-m)} e^-, \quad (4)$$

Eq. 4 gives the number of source counts per exposure, and  $m$  represents the AB magnitude of the object for a given band.  $b(\lambda) e^-$  is a baseline flux at AB magnitude  $m = 18.3$  determined by using the routine `galsim.wfirst.getBandpasses (AB_zeropoint=True)`, which uses a exposure time of 168.1 seconds by default.

Notice that in our simulations we have neglected the main sources of noise that would affect the HLS—zodiacal background, thermal emission, and read noise—which would make all images slightly more nonlinear. Calculations performed with the WFIRST Exposure Time Calculator v.14<sup>15</sup> (Hirata et al. 2012) in weak lensing mode (ETC-WL) by Spergel et al. 2015 in the F184 band (a conservative case) show that the combined contribution due to these backgrounds sources would be approximately  $130 e^-$  per pixel for a 174 seconds exposure (comparable to the 168.1 exposure time assumed in this work), negligible compared with the values used in our simulations (Table 1).

Total and peak flux values at each filter per postage stamp are shown in Table 1. The brightest magnitude used was AB  $m = 18.3$ , based on the peak value of the PSF profile in the Y106 band when rendered into a postage stamp at the native pixel scale and placed at the center of the pixel:  $\sim 1.00237 \times 10^5$  electrons, representing about 90% of the typical full well depth in the pixels of the H4RG detectors— $\sim 1.1 \times 10^5$  electrons. Note that this peak value is an upper limit and will vary for a slightly offset profile. For our calculations, we randomize the centroid of the profile within the native scale pixel. In addition, since NL is a function of signal, and since `GalSim` conserves total flux when changing pixel scales, the total flux in the higher resolution image must be multiplied by a factor of  $N^2$  to preserve the appropriate response per pixel to this effect, correcting for the fact that the new image has a factor of  $N^2$  more pixels than the one created at the native scale.

For simplicity of analysis, the postage stamps are noiseless and no other sensor effect is applied. After convolving the PSF profile with a pixel of the size of the native scale and rendering

---

<sup>15</sup><https://wfirst.ipac.caltech.edu/sims/tools/wfDepc/wfDepc.html>

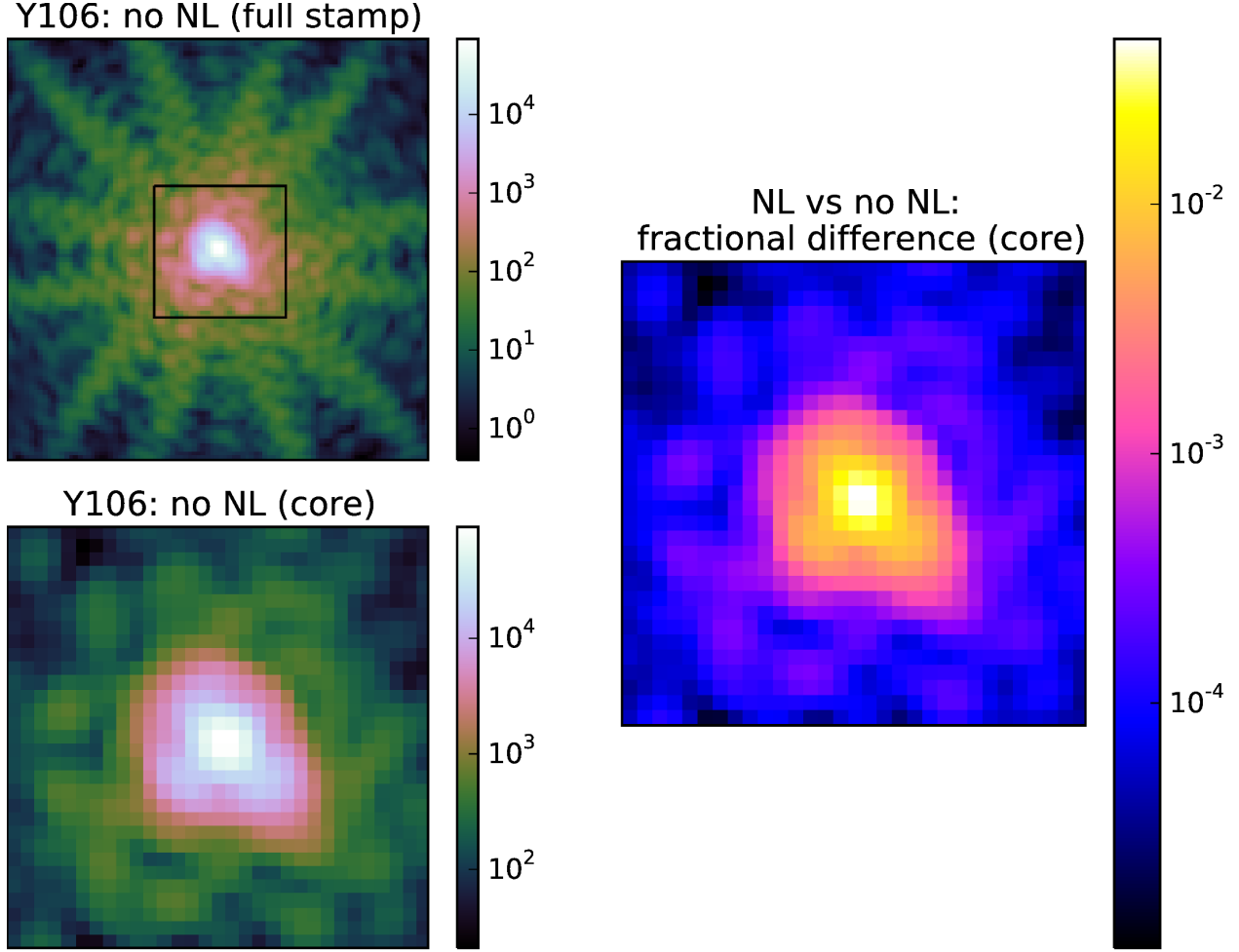


Fig. 1.— Example of the WFIRST PSF profiles in the Y106 band created by the `galsim.wfirst.getPSF` method. The profile is drawn on a postage stamp with a size of  $1.5k \times 1.5k$  pixels ( $k = 64$ ) and a resolution of  $p/N$ , with  $p = 0.11$  arcseconds and  $N = 3$ . Before drawing the profiles, they are first convolved with a pixel response of size  $p$  and given a flux obtained through the use of the `galsim.wfirst.getBandpasses` (`AB_zeropoint=True`) routine at an AB magnitude of 18.3 (at an exposure time of 168.1 seconds). However, to preserve the correct response to NL, the higher-resolution image has  $N^2$  more total flux. The NL effect is applied at the native pixel scale  $p$ , and the centroid of the profile randomized within the pixel at this same scale (in this example the centroid and the pixel center coincide). The upper left panel shows the full postage stamp PSF image without the NL applied, while the lower left panel shows a zoom into the core (squared central region in upper left panel) of 30 by 30 high resolution pixels. The right-hand side image shows the fractional difference between the PSF without the NL applied and a PSF with NL using  $\beta_0$  for the model parameter.

the image at the high-resolution scale, NL is applied by using Eq. 1 through the use of the `galsim.image.applyNonlinearity` method.

Fig. 1 shows an example of the PSF profiles and postage stamps created for our simulations (J129 band). The effect of NL (at the nominal  $\beta_0$ ) is small, and the difference image reveals that the attenuation in the flux is of the order of a few percent, mainly for the larger signals found at the core of the PSF. Kannawadi et al. 2015 present more details on the `galsim.wfirst` module, along with examples of the PSF profiles that can be generated in all 6 WFIRST filters.

### 3.2. PSF size and shape measurement

The accurate determination of PSF properties such as size and ellipticity is crucial to avoid the propagation of systematic biases in cosmological parameters through the use of weak gravitational lensing (Paulin-Henriksson et al. 2008, Paulin-Henriksson et al. 2009, Massey et al. 2013, Cropper et al. 2013). In general, the problem of galaxy and PSF shape measurements for accurate weak lensing is non-trivial, and even when the PSF is perfectly known, shape measurement algorithms can introduce biases. Several shape measurements algorithms—ranging from model-fitting methods to particular combinations of weighted central moments and bayesian techniques—have been and are being investigated in order to produce accurate shear estimators that satisfy the requirements of current and future WL surveys (Mandelbaum et al. 2015).

To measure the profile shapes and size, we use the adaptive moments method (Bernstein and Jarvis 2002, Hirata and Seljak 2003), which is already implemented in `GalSim` as `galsim.hsm.FindAdaptiveMom()`. Adaptive moments are effectively weighted by an elliptical Gaussian. At first they are calculated by computing moments weighted by a circular Gaussian with some arbitrary size. Then the output moments are used to define a new elliptical Gaussian that will act as a new weight function. The process is iteratively repeated until the output moments are the same as those of the weight function. The ellipticity  $e = e_1 + ie_2$  and size  $R$  are then defined as

$$e_1 = \frac{M_{xx} - M_{yy}}{M_{xx} + M_{yy}} \quad (5)$$

$$e_2 = \frac{2M_{xy}}{M_{xx} + M_{yy}} \quad (6)$$

$$R = \det[\mathbf{M}]^{1/4} \quad (7)$$

where the centroid  $\bar{\mathbf{x}}$  and moment matrix  $\mathbf{M}$  of an image are defined as

$$\bar{\mathbf{x}} = \frac{\int d^2\mathbf{x} w(\mathbf{x})\mathbf{x}I(\mathbf{x})}{\int d^2\mathbf{x} w(\mathbf{x})I(\mathbf{x})} \quad (8)$$

$$M_{ij} = \frac{\int d^2\mathbf{x} (\mathbf{x} - \bar{\mathbf{x}})_i(\mathbf{x} - \bar{\mathbf{x}})_j w(\mathbf{x})I(\mathbf{x})}{\int d^2\mathbf{x} w(\mathbf{x})I(\mathbf{x})} \quad (9)$$

for an elliptical Gaussian weight function  $w(\mathbf{x})$ . We note that adaptive moments are particularly sensitive to the core of the PSF when the PSF profile is diffraction-limited, and therefore they should be particularly sensitive to NL effects.

### 3.3. Changes in size and ellipticity induced by NL

We quantify the effect of nonlinearity by measuring the fractional change in size and the absolute change in ellipticity of the PSF profiles,<sup>16</sup> in the 4 filters of the HLS of WFIRST and for several values of the NL model parameter  $\beta$ . We calculate the quantities  $\Delta e_1$ ,  $\Delta e_2$ , and  $\frac{\Delta R}{R}$ , which are defined as the difference between the measured ellipticity or size after the effect (NL) is applied and the reference values measured before (represented by the subscript “0”) the application of NL:

$$\Delta e_i \equiv e_i - e_{i,0}, \quad i \in [1, 2] \quad (10)$$

$$\frac{\Delta R}{R} \equiv \frac{R - R_0}{R_0} \quad (11)$$

In this way, we are less sensitive to the details (and possible biases) of the shape measurement algorithm, since we only care about relative changes induced by the detector effect.

The basic simulation process is summarized by the following steps:

1. Create a WFIRST PSF surface brightness profile with a given flux as prescribed by Eq. 4, and convolve the PSF profile with a top-hat pixel response with the size of the native scale of the WFIRST FPA ( $p = 0.11$  arcseconds per pixel) to produce an effective PSF.
2. Draw the effective PSF profile in a noiseless postage stamp of size  $1.5k$  by  $1.5k$  ( $k = 64$ ) pixels at a higher resolution of  $p/N$ , with  $N = 3$ , and multiply the resulting image by  $N^2$ . In this step, NL is not yet applied, but it will be done so in a later step, so the flux still needs to be adjusted. The centroid of the profile is uniformly randomized within the native resolution pixel.
3. Create another image of the effective PSF at a higher resolution and with the flux adjusted as in step 2. Apply the nonlinearity to the postage stamps according to the transformation  $I \mapsto I - \beta I^2$  (*c.f.* Eq. 1).

---

<sup>16</sup>In WL, before measuring a given galaxy shape the PSF has to be corrected. By propagating the errors in the determination of the size and ellipticity of the PSF, it can be shown (see, *e.g.*, Paulin-Henriksson et al. 2008) that the error in the measurement of the source galaxy ellipticity is—to first order—given by a linear combination of the fractional PSF size error and the absolute PSF ellipticity error, which are the metrics we have chosen to study in this work.

4. Use the adaptive moments algorithm to measure the shape  $e_0 = (e_{1,0}, e_{2,0})$  and size  $R_0$  of the profile without NL to have as baseline reference.
5. Measure the shape and size of the object with the sensor effect applied, and calculate the quantities  $\Delta e_1$ ,  $\Delta e_2$ , and  $\frac{\Delta R}{R}$ , as defined in Eqs. 10 and 11.
6. Repeat steps 1 to 5, averaging over 100 centroid realizations. The values reported will be the mean and the standard deviation over these realizations (see Fig. 2 and Fig. 3).
7. To study the impact of spatial variability in  $\beta$ , repeat steps 1 to 6 and assume that  $\beta$  for each high-resolution pixel can be drawn from a Gaussian distribution with some mean  $\beta$  and variance  $\sigma_\beta^2$ . Over  $M$  realizations (for a fixed centroid), calculate the dispersion values  $\sigma_{\Delta e_1}$ ,  $\sigma_{\Delta e_2}$ , and  $\sigma_{\Delta R/R}$  as a function of  $\sigma_\beta$ . In our simulations we use  $M = 100$  (see Fig. 4 and Fig. 5).

## 4. Results

### 4.1. Biases in ellipticity and size

Fig. 2 shows the fractional change in PSF size and the absolute error in PSF ellipticity as a function of the mean nonlinearity parameter  $\beta$ , for different bandpass filters at fixed AB magnitude of 18.3 in each band, consistent with the magnitude of nearly saturated stars in the HLS. We note that the flux in each band will depend on the particular stellar spectral energy distribution (SED), and we would need to specify a particular SED to go from one reference band to other bands. For simplicity, we are performing our calculations based on a grid of AB magnitudes in different filters.

In the H158 band, the mean nominal value of  $\beta_0 = 5 \times 10^{-7}/e^-$  induces errors in the size and ellipticity of about  $1 \times 10^{-2}$  and  $2 \times 10^{-3}$  respectively, larger than the required values of  $10^{-3}$  and  $4.5 \times 10^{-4}$  on the knowledge of the size and ellipticity of the PSF in order not to bias cosmological parameter inferences from WL experiments (§1). As the  $\beta$  parameter is increased, the amplitude of the errors increases approximately in a linear manner within the domain of  $\beta$  values considered.

Since  $\Delta R/R$  and  $\Delta e$  are approximately linear in  $\beta$ , we can condense this information by simply plotting the slope for various filters and star magnitudes. This is shown in Fig. 3, which presents  $\Delta R/R/\beta$  and  $\Delta e/\beta$  (the slopes in Fig. 2) vs  $m$  for each of the four filters of the HLS. From Fig. 3, it is possible to estimate the precision to which  $\beta$  would have to be calibrated in order to limit the relative size and ellipticity bias of a star with a given magnitude. In particular, letting  $(\beta - \beta_0)/\beta_0 \equiv \Delta\beta/\beta_0$  represent the fractional error in the measurement of a given value of  $\beta_0$ , we have:

$$\frac{\Delta R/R}{\Delta\beta} = c \quad \Rightarrow \quad \frac{\Delta\beta}{\beta_0} = \frac{\Delta R/R}{c\beta_0} \quad (12)$$

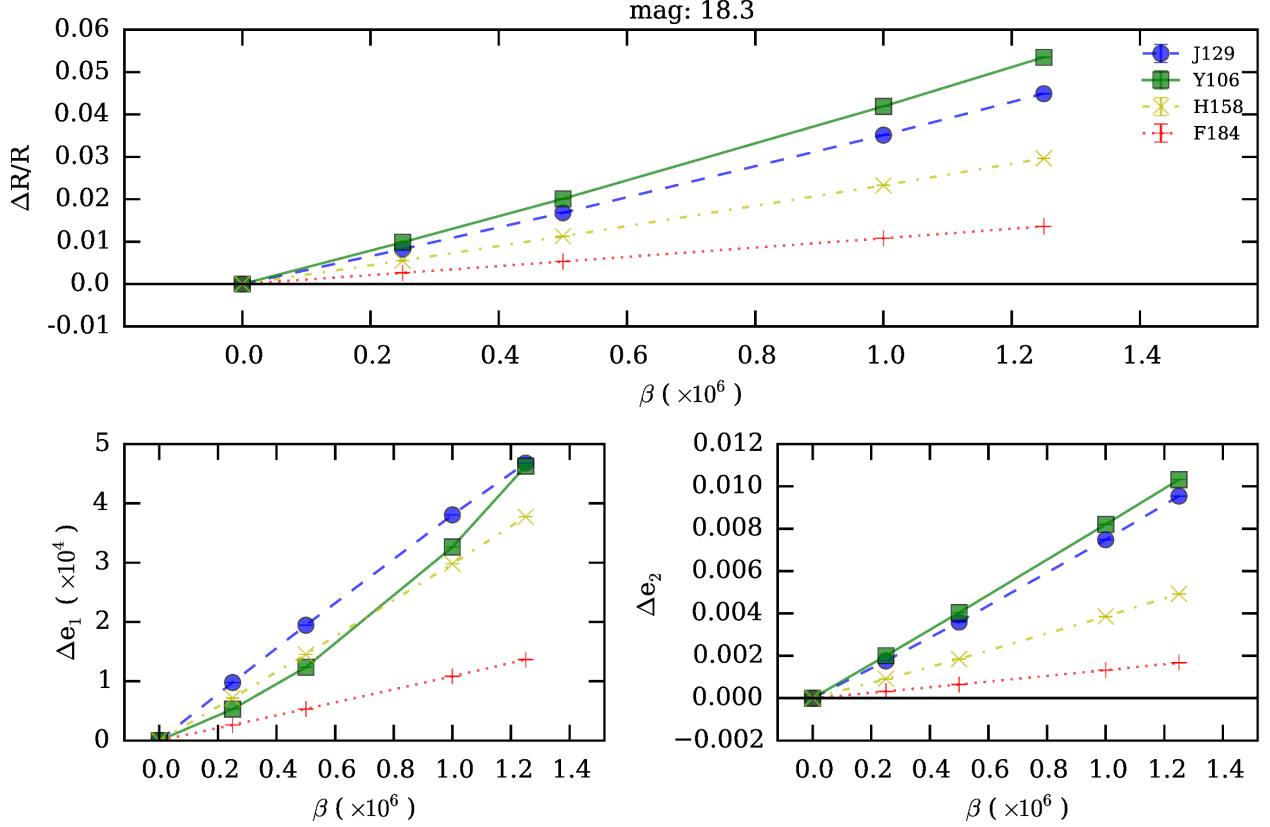


Fig. 2.— Fractional error in PSF size (upper panel) and absolute error in PSF ellipticity components (lower panels) as a function of the mean nonlinearity parameter  $\beta$  for the WFIRST PSF, in four the four HSL filters (J129, Y106, H158, and F184), and an AB magnitude of 18.3 at 168.1 seconds of exposure time (similar plots were found for other magnitude values). Each point is the mean over 100 realizations of uniformly distributed random centroid shifts within the high resolution images ( $N = 3$ ), and the associated error bars (too small to be seen) represent the standard deviation of the realizations.

In Eq.12,  $c$  represents the ordinate value in Fig. 3 for a given magnitude, and we have replaced  $\Delta R/R/\beta$  by  $\Delta R/R/\Delta\beta$  since the linearity in the bias in  $\Delta R/R$  and  $\Delta e$  vs  $\beta$  for all magnitudes makes the choice of the expansion point of the approximation by Taylor expansion unimportant (*i.e.*, it does not matter if the expansion is around  $\beta = 0$  or  $\beta = \beta_0$ ). An analogous equation to Eq. 12 can be written for the error in the ellipticity if  $\Delta R/R$  is replaced by  $\Delta e$ .

Under these conditions, Fig. 3 shows that for the brightest stars in our range, to limit the bias of  $\Delta R/R$  ( $\Delta e$ ) in the H158 band to  $10^{-4}$  ( $4.7 \times 10^{-5}$ )—about 10% of the estimated WFIRST error budgets,  $\beta$  must be calibrated to  $\sim 1\%$  ( $\sim 2.4\%$ ) (using  $c \sim 2 \times 10^4 e^-$  at  $m = 18.3$  from the upper panel of Fig. 3,  $c \sim 4000$  at  $m = 18.3$  from the lower right panel of the same figure, and  $\beta_0 = 5 \times 10^{-7}/e^-$ ). For this error tolerance, if the required calibration cannot be achieved, then

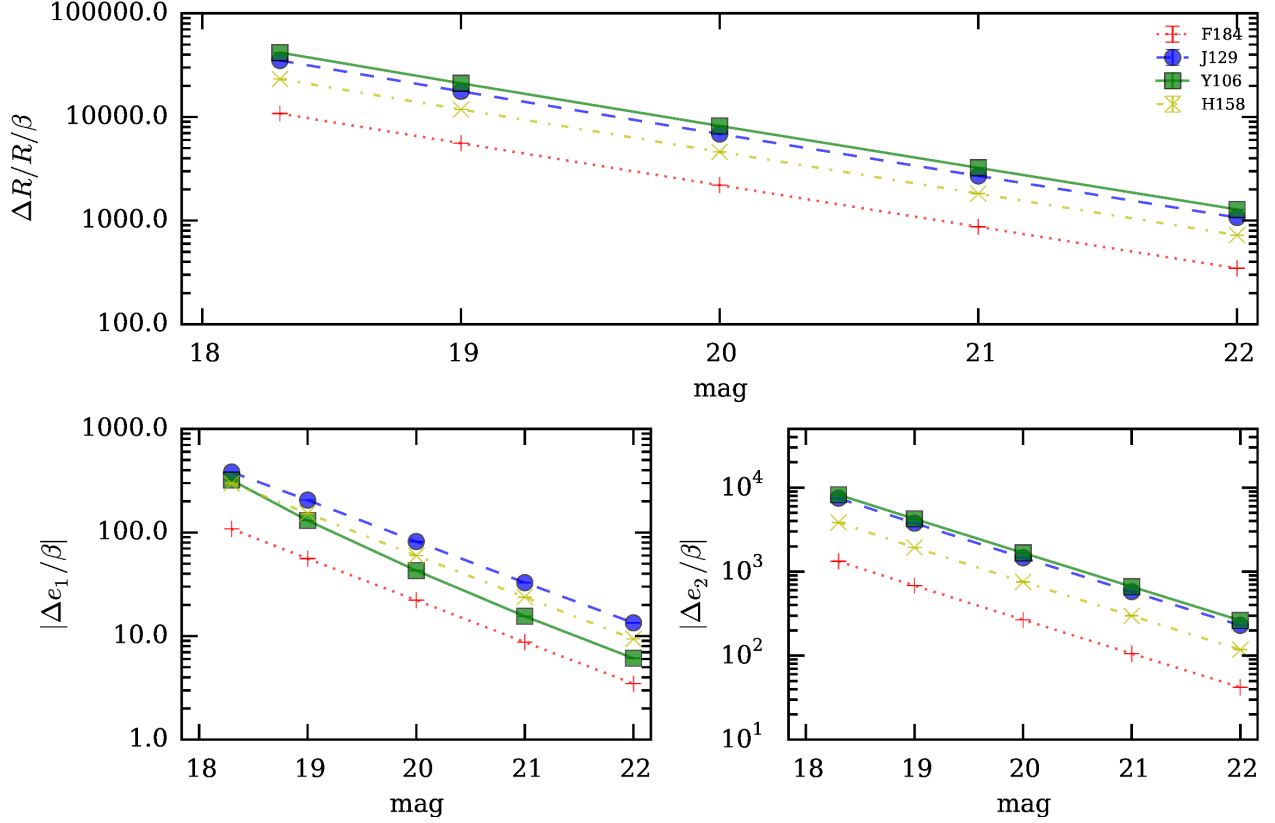


Fig. 3.— Fractional error in PSF size and absolute error in PSF ellipticity components normalized by the NL model parameter  $\beta$ , as a function of magnitude for the four HSL filters (J129, Y106, H158, and F184). The ordinate axis in each plot represents the slope of the linear relationships in Fig. 2, derived by linear fitting of points around the vicinity of  $\beta_0$  in each curve of that figure.

one must find a higher star magnitude with a less strict requirement. Our choice of error tolerance here is somewhat arbitrary and only for illustration, and Eq. 12 and Fig. 3 should be used to derive detector requirements once true PSF requirements are known.

The trends in Fig. 3 are clearly well-described by a power law with a common slope for the various filters. We fit a function only to the PSF size trend since it will be a more robust characteristic of the survey, whereas ellipticity can have relatively wide spatial variations. For a power law of the form

$$\frac{\Delta R/R}{\beta} = A_F 10^{B_F(m-m_0)} \quad (m_0 = 20), \quad (13)$$

the parameters  $A_F$  and  $B_F$  for each filter F are listed in Table 2.

## 4.2. Impacts of spatial variability of $\beta$

We also studied the impact on  $\Delta e$  and  $\Delta R/R$  due to the dispersion in the  $\beta$  parameter. Due to non-uniformities in fabrication, each pixel can have a different NL coefficient, and biases in the measurement of PSF properties could be introduced if a mean response curve is used to calibrate NL instead of a single curve per pixel. Fig. 4 shows the dispersion over  $M = 100$  realizations (for a fixed centroid) in the metrics  $\Delta e_1$ ,  $\Delta e_2$ , and  $\Delta R/R$  as a function of the standard deviation  $\sigma_{\beta_0}$ , assuming that the coefficient  $\beta$  is drawn from a distribution of the form  $\mathcal{N} \sim (\beta_0, \sigma_{\beta_0})$ .

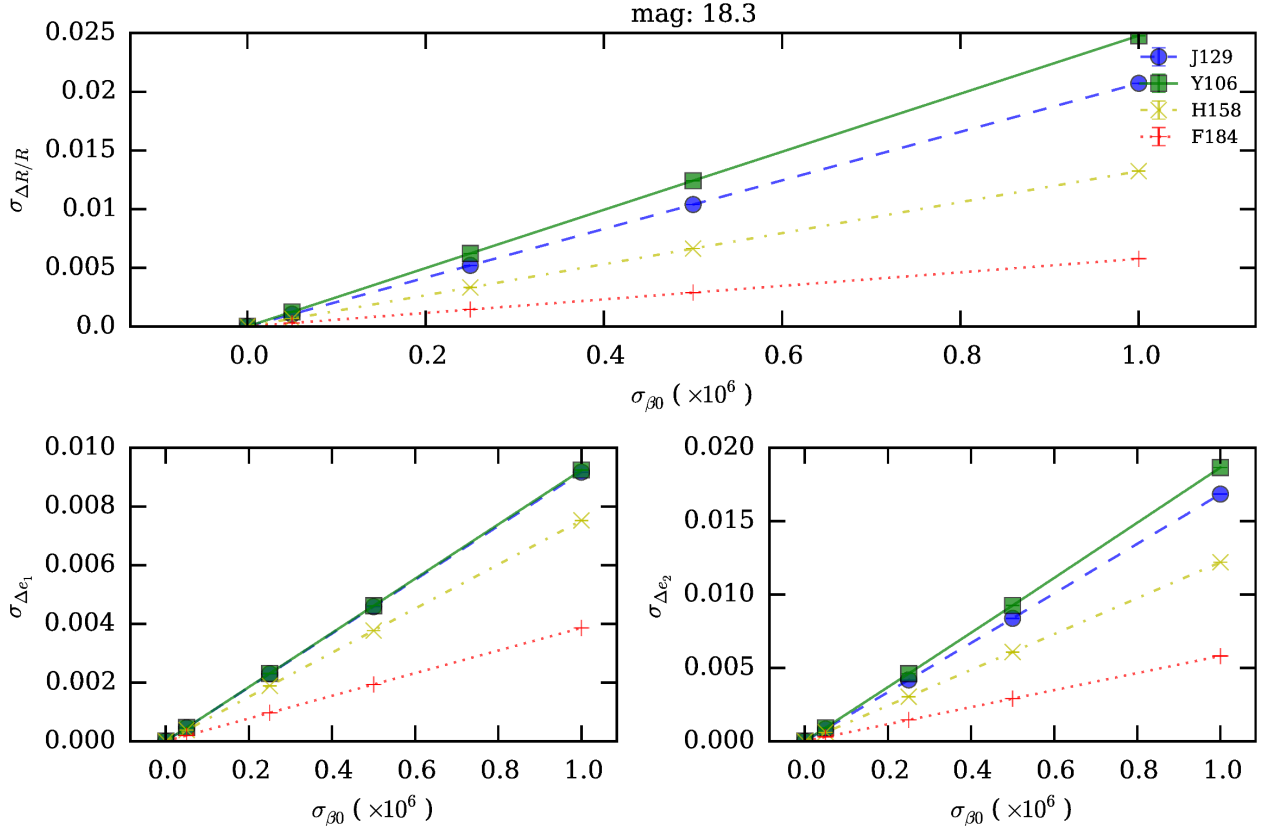


Fig. 4.— Impact of spatial variability in the  $\beta_0$  parameter, quantified as the standard deviation over  $M = 100$  realizations (for a fixed centroid) in  $\Delta e_1$ ,  $\Delta e_2$ , and  $\Delta R/R$  as a function of the standard deviation  $\sigma_{\beta_0}$ .

We found that the results in Fig. 4 are insensitive to the nominal  $\beta$  and therefore, in general,  $\sigma_{\beta}$  can be treated as an error on  $\beta$  estimation. The linear relationships in Fig. 4 also allows us to plot the slope of each curve for different magnitudes, as was done in Fig. 3, and therefore analogous equations to Eqn. 12 can be used to derive requirements on the maximum tolerable dispersion in size and ellipticity errors given a particular set of parameters and requirements. The results are



shown in Fig. 5. We also fitted a model of the form

$$\frac{\sigma_{\Delta R/R}}{\sigma_{\beta}} = A_F 10^{B_F(m-m_0)} \quad (m_0 = 20) \quad (14)$$

for the PSF size trends in Fig. 5, as was done above for Fig. 3 (*c.f.*, Eqn. 13). The fit parameters are presented in Table 2 as well.

## 5. Conclusion

We have used the WFIRST module in `GalSim` to study the impact on PSF measurement for weak lensing science due to the nonlinearity in the conversion of charge to voltage in near-infrared hybrid CMOS detectors (such as those that will be used in the Wide Field Imager of the WFIRST mission). The PSF profiles created by the `galsim.wfirst` module possess several of the design characteristics of the expected PSF of the mission, such as optical aberrations and pixel scale. The module can also be used to assign the PSF profiles fluxes per pixel consistent with the expected brightness of the HLS.

Voltage nonlinearity—as studied in this work—encompasses the linearity due to the shrinking of the depletion region at the p-n junction as charge accumulates, and the deviation from linearity originating in the multiplexer gain. It depends on the total integrated signal (fluence), and it is more dominant at high signals than other types of nonlinearity such as reciprocity failure, which dominates at lower signals. As such, NL will tend to depress the flux in the core of the PSF relative to the wings in bright stars that are usually used for PSF estimation, introducing errors when deconvolving the PSF at the interpolated galaxy positions.

To model NL, we have used a single, one-parameter transfer function quadratic in the charge  $Q$  (Eq. 1). We have studied the consequences of NL in isolation by using the relationship in Eq. 1, not considering other sensor effects, and neglecting sources of noise such as zodiacal background, thermal emission, and read noise (which would produce a negligible contribution). We have used the metrics  $\Delta R/R$  and  $\Delta e$  to assess the impact of NL on PSF size and ellipticity, which have to be controlled to  $\sim O(10^{-4})$  or better, for different values of the parameter space at hand ( $\beta$ , PSF

Band	size bias (Fig. 3)		size scatter (Fig. 5)	
	$A_F$	$B_F$	$A_F$	$B_F$
Y106	8322	-0.4086	5057	-0.4045
J129	6958	-0.4089	4215	-0.4050
H158	4668	-0.4069	2711	-0.4038
F184	2209	-0.4035	1194	-0.4018

Table 2: Parameters resulting from fitting the curves in the upper panel of Figs. 3 and 5 to power-law functions of the form  $\Delta R/R/\beta = A_F 10^{B_F(m-20)}$  and  $\sigma_{\Delta R/R}/\sigma_{\beta} = A_F 10^{B_F(m-20)}$ , respectively.

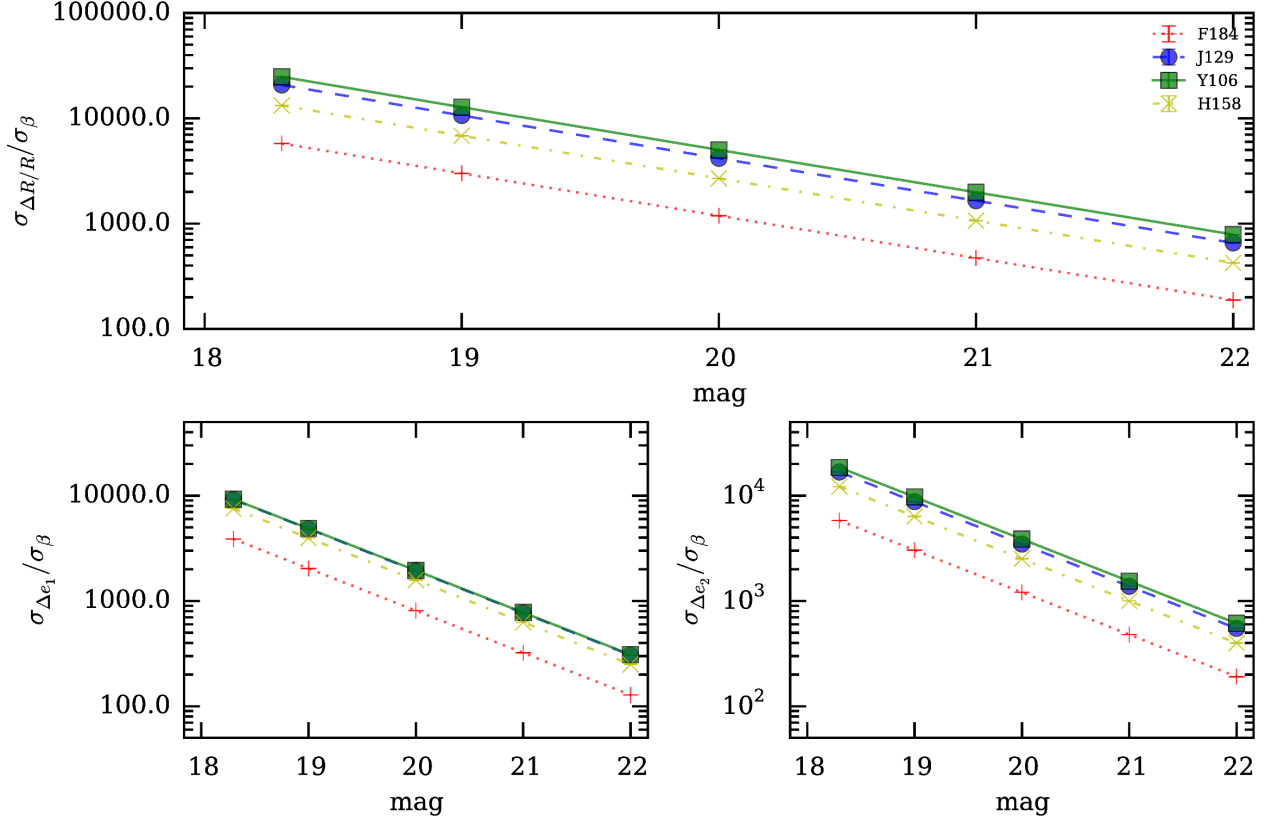


Fig. 5.— Standard deviation of the fractional error in PSF size and of the absolute error in PSF ellipticity components normalized by the NL model parameter  $\beta$ , as a function of magnitude for the four HSL filters (J129, Y106, H158, and F184).

magnitude, and bandpass filters to be used in WFIRST WL analyses). We have also studied the effects of spatial variation of the  $\beta$  coefficient along the pixel array, by assuming that it follows a Gaussian distribution.

For the nominal value  $\beta_0$  assumed in this work, we find that NL induces errors in PSF size and shape larger to what is tolerable by accurate WL measurements. For an example set of assumed requirements on PSF size and ellipticity ( $10^{-4}$  and  $4.7 \times 10^{-5}$ , respectively), we find that  $\beta$  should be calibrated to about 1% to 2.4% (H158 band). However, the results derived in this study (Eq. 12, Fig. 3, and Fig. 5) can be used to derive requirements on NL for the WFIRST detectors for a different set of tolerances on PSF properties. It is important to note that new measurements on the actual H4RG detector that will be used by the WFIRST imager will have to be performed in order to determine the mean value of  $\beta$  and its dispersion.

Nonlinearity measurements are usually performed by looking at signal as a function of exposure time at a constant flux (and subtracting dark frames at the appropriate times), which is sensible to any gain dependence on fluence. These measurements are normally subject to other effects such

as inaccuracies in the readout time, persistence, reciprocity failure, and time-dependent changes in the electronic offset due to self-heating effects in the multiplexer. Despite these challenges, the mean non-linearity signal can usually be characterized to a precision of 5–10%. Thus it is not obvious that a typical NL calibration program will be sufficient for WL with WFIRST without more careful study and error budgeting. To ensure that voltage nonlinearity in the WFIRST H4RG detectors can be calibrated to the levels demanded by WL science, NL characterization will be crucial through the use of facilities such as the Detector Characterization Laboratory<sup>17</sup> for rigorous calibration studies and the Precision Projector Laboratory (PPL, Seshadri et al. 2013, Shapiro et al. 2013)<sup>18</sup> for validating the impact of NL on shape measurement.

We thank Chris Hirata, Jeff Kruk, Dave Content and the WFIRST detector requirements working group for useful discussions. AAP is supported by the Jet Propulsion Laboratory. CS and JR are being supported in part by the Jet Propulsion Laboratory. The research was carried out at the Jet Propulsion Laboratory, California Institute of Technology, under a contract with the National Aeronautics and Space Administration.

© 2016. All rights reserved.

## REFERENCES

- A. Albrecht, G. Bernstein, R. Cahn, W. L. Freedman, J. Hewitt, W. Hu, J. Huth, M. Kamionkowski, E. W. Kolb, L. Knox, J. C. Mather, S. Staggs, and N. B. Suntzeff. Report of the Dark Energy Task Force. *ArXiv Astrophysics e-prints*, September 2006.
- A. Amara and A. Réfrégier. Systematic bias in cosmic shear: extending the Fisher matrix. *MNRAS*, 391:228–236, November 2008. doi: 10.1111/j.1365-2966.2008.13880.x.
- James W. Beletic, Richard Blank, David Gulbransen, Donald Lee, Markus Loose, Eric C. Piquette, Thomas Sprafke, William E. Tennant, Majid Zandian, and Joseph Zino. Teledyne imaging sensors: infrared imaging technologies for astronomy and civil space, 2008.
- G. M. Bernstein and R. Armstrong. Bayesian lensing shear measurement. *MNRAS*, 438:1880–1893, February 2014. doi: 10.1093/mnras/stt2326.
- G. M. Bernstein and M. Jarvis. Shapes and Shears, Stars and Smears: Optimal Measurements for Weak Lensing. *AJ*, 123:583–618, February 2002. doi: 10.1086/338085.

---

<sup>17</sup><https://detectors.gsfc.nasa.gov/DCL/>

<sup>18</sup>The PPL is a joint project between NASA Jet Propulsion Laboratory and Caltech which validates image sensor behavior using laboratory emulations of astronomical data.

- G. M. Bernstein, R. Armstrong, C. Krawiec, and M. C. March. An accurate and practical method for inference of weak gravitational lensing from galaxy images. *ArXiv e-prints*, August 2015.
- E. Bertin. Automatic Astrometric and Photometric Calibration with SCAMP. In C. Gabriel, C. Arviset, D. Ponz, and S. Enrique, editors, *Astronomical Data Analysis Software and Systems XV*, volume 351 of *Astronomical Society of the Pacific Conference Series*, page 112, July 2006.
- T. Biesiadzinski, W. Lorenzon, R. Newman, M. Schubnell, G. Tarlé, and C. Weaverdyck. Measurement of Reciprocity Failure in Near-Infrared Detectors. *PASP*, 123:179–186, February 2011. doi: 10.1086/658282.
- R. C. Bohlin, D. J. Lindler, and A. Riess. Grism Sensitivities and Apparent Non-Linearity. Technical report, May 2005.
- M. Cropper, H. Hoekstra, T. Kitching, R. Massey, J. Amiaux, L. Miller, Y. Mellier, J. Rhodes, B. Rowe, S. Pires, C. Saxton, and R. Scaramella. Defining a weak lensing experiment in space. *MNRAS*, 431:3103–3126, June 2013. doi: 10.1093/mnras/stt384.
- T. Diehl and Dark Energy Survey Collaboration. The Dark Energy Survey Camera (DECam). *Physics Procedia*, 37:1332–1340, 2012. doi: 10.1016/j.phpro.2012.02.472.
- A. S. Fruchter. A New Method for Band-limited Imaging with Undersampled Detectors. *PASP*, 123:497–502, April 2011. doi: 10.1086/659313.
- A. S. Fruchter and R. N. Hook. Drizzle: A Method for the Linear Reconstruction of Undersampled Images. *PASP*, 114:144–152, February 2002. doi: 10.1086/338393.
- L. Girardi, M. Barbieri, M. A. T. Groenewegen, P. Marigo, A. Bressan, H. J. Rocha-Pinto, B. X. Santiago, J. I. B. Camargo, and L. N. da Costa. TRILEGAL, a TRIdimensional model of thE GALaxy: Status and Future. *Astrophysics and Space Science Proceedings*, 26:165, 2012. doi: 10.1007/978-3-642-18418-5\_17.
- J. Green, P. Schechter, C. Baltay, R. Bean, D. Bennett, R. Brown, C. Conselice, M. Donahue, X. Fan, B. S. Gaudi, C. Hirata, J. Kalirai, T. Lauer, B. Nichol, N. Padmanabhan, S. Perlmutter, B. Rauscher, J. Rhodes, T. Roellig, D. Stern, T. Sumi, A. Tanner, Y. Wang, D. Weinberg, E. Wright, N. Gehrels, R. Sambruna, W. Traub, J. Anderson, K. Cook, P. Garnavich, L. Hillenbrand, Z. Ivezic, E. Kerins, J. Lunine, P. McDonald, M. Penny, M. Phillips, G. Rieke, A. Riess, R. van der Marel, R. K. Barry, E. Cheng, D. Content, R. Cutri, R. Goullioud, K. Grady, G. Helou, C. Jackson, J. Kruk, M. Melton, C. Peddie, N. Rioux, and M. Seiffert. Wide-Field InfraRed Survey Telescope (WFIRST) Final Report. *ArXiv e-prints*, August 2012.
- D. Gruen, G. M. Bernstein, M. Jarvis, B. Rowe, V. Vikram, A. A. Plazas, and S. Seitz. Characterization and correction of charge-induced pixel shifts in DECam. *Journal of Instrumentation*, 10:C05032, May 2015. doi: 10.1088/1748-0221/10/05/C05032.

- B. Hilbert. Non-Linearity Correction Algorithm for the WFC3 IR Channel. Technical report, May 2004.
- B. Hilbert. WFC3 TV3 Testing: IR Channel Nonlinearity Correction. Technical report, 2008.
- B. Hilbert. Updated non-linearity calibration method for WFC3/IR. Technical report, July 2014.
- C. Hirata and U. Seljak. Shear calibration biases in weak-lensing surveys. *MNRAS*, 343:459–480, August 2003. doi: 10.1046/j.1365-8711.2003.06683.x.
- C. M. Hirata, N. Gehrels, J.-P. Kneib, J. Kruk, J. Rhodes, Y. Wang, and J. Zoubian. The WFIRST Galaxy Survey Exposure Time Calculator. *ArXiv e-prints*, April 2012.
- H. Hoekstra and B. Jain. Weak gravitational lensing and its cosmological applications. *Annual Review of Nuclear and Particle Systems*, 58:99–123, 2008.
- D. Huterer, M. Takada, G. Bernstein, and B. Jain. Systematic errors in future weak-lensing surveys: requirements and prospects for self-calibration. *MNRAS*, 366:101–114, February 2006. doi: 10.1111/j.1365-2966.2005.09782.x.
- Z. Ivezić, J. A. Tyson, B. Abel, E. Acosta, R. Allsman, Y. AlSayyad, S. F. Anderson, J. Andrew, R. Angel, G. Angeli, R. Ansari, P. Antilogus, K. T. Arndt, P. Astier, E. Aubourg, T. Axelrod, D. J. Bard, J. D. Barr, A. Barrau, J. G. Bartlett, B. J. Bauman, S. Beaumont, A. C. Becker, J. Becla, C. Beldica, S. Bellavia, G. Blanc, R. D. Blandford, J. S. Bloom, J. Bogart, K. Borne, J. F. Bosch, D. Boutigny, W. N. Brandt, M. E. Brown, J. S. Bullock, P. Burchat, D. L. Burke, G. Cagnoli, D. Calabrese, S. Chandrasekharan, S. Chesley, E. C. Cheu, J. Chiang, C. F. Claver, A. J. Connolly, K. H. Cook, A. Cooray, K. R. Covey, C. Cribbs, W. Cui, R. Cutri, G. Daubard, G. Daues, F. Delgado, S. Digel, P. Doherty, R. Dubois, G. P. Dubois-Felsmann, J. Durech, M. Eracleous, H. Ferguson, J. Frank, M. Freemon, E. Gangler, E. Gawiser, J. C. Geary, P. Gee, M. Geha, R. R. Gibson, D. K. Gilmore, T. Glanzman, I. Goodenow, W. J. Gressler, P. Gris, A. Guyonnet, P. A. Hascall, J. Haupt, F. Hernandez, C. Hogan, D. Huang, M. E. Huffer, W. R. Innes, S. H. Jacoby, B. Jain, J. Jee, J. G. Jernigan, D. Jevremovic, K. Johns, R. L. Jones, C. Juramy-Gilles, M. Juric, S. M. Kahn, J. S. Kalirai, N. Kallivayalil, B. Kalmbach, J. P. Kantor, M. M. Kasliwal, R. Kessler, D. Kirkby, L. Knox, I. Kotov, V. L. Krabbendam, S. Krughoff, P. Kubanek, J. Kuczewski, S. Kulkarni, R. Lambert, L. Le Guillou, D. Levine, M. Liang, K. Lim, C. Lintott, R. H. Lupton, A. Mahabal, P. Marshall, S. Marshall, M. May, R. McKercher, M. Migliore, M. Miller, D. J. Mills, D. G. Monet, M. Moniez, D. R. Neill, J. Nief, A. Nomerotski, M. Nordby, P. O’Connor, J. Oliver, S. S. Olivier, K. Olsen, S. Ortiz, R. E. Owen, R. Pain, J. R. Peterson, C. E. Petry, F. Pierfederici, S. Pietrowicz, R. Pike, P. A. Pinto, R. Plante, S. Plate, P. A. Price, M. Prouza, V. Radeka, J. Rajagopal, A. Rasmussen, N. Regnault, S. T. Ridgway, S. Ritz, W. Rosing, C. Roucelle, M. R. Rumore, S. Russo, A. Saha, B. Sassolas, T. L. Schalk, R. H. Schindler, D. P. Schneider, G. Schumacher, J. Sebag, G. H. Sembroski, L. G. Seppala, I. Shipsey, N. Silvestri, J. A.

Smith, R. C. Smith, M. A. Strauss, C. W. Stubbs, D. Sweeney, A. Szalay, P. Takacs, J. J. Thaler, R. Van Berg, D. Vanden Berk, K. Vetter, F. Virieux, B. Xin, L. Walkowicz, C. W. Walter, D. L. Wang, M. Warner, B. Willman, D. Wittman, S. C. Wolff, W. M. Wood-Vasey, P. Yoachim, H. Zhan, and for the LSST Collaboration. LSST: from Science Drivers to Reference Design and Anticipated Data Products. *ArXiv e-prints*, May 2008.

M. Jarvis. Challenges for precision shape measurements. *Journal of Instrumentation*, 9(03):C03017, 2014. URL <http://stacks.iop.org/1748-0221/9/i=03/a=C03017>.

M. Jarvis, E. Sheldon, J. Zuntz, T. Kacprzak, S. L. Bridle, A. Amara, R. Armstrong, M. R. Becker, G. M. Bernstein, C. Bonnett, C. Chang, R. Das, J. P. Dietrich, A. Drlica-Wagner, T. F. Eifler, C. Gangkofner, D. Gruen, M. Hirsch, E. M. Huff, B. Jain, S. Kent, D. Kirk, N. MacCrann, P. Melchior, A. A. Plazas, A. Refregier, B. Rowe, E. S. Rykoff, S. Samuroff, C. Sánchez, E. Suchyta, M. A. Troxel, V. Vikram, T. Abbott, F. B. Abdalla, S. Allam, J. Annis, A. Benoit-Lévy, E. Bertin, D. Brooks, E. Buckley-Geer, D. L. Burke, D. Capozzi, A. Carnero Rosell, M. Carrasco Kind, J. Carretero, F. J. Castander, M. Crocce, C. E. Cunha, C. B. D’Andrea, L. N. da Costa, D. L. DePoy, S. Desai, H. T. Diehl, P. Doel, A. Fausti Neto, B. Flaugher, P. Fosalba, J. Frieman, E. Gaztanaga, D. W. Gerdes, R. A. Gruendl, G. Gutierrez, K. Honscheid, D. J. James, K. Kuehn, N. Kuropatkin, O. Lahav, T. S. Li, M. Lima, M. March, P. Martini, R. Miquel, J. J. Mohr, E. Neilsen, B. Nord, R. Ogando, K. Reil, A. K. Romer, A. Roodman, M. Sako, E. Sanchez, V. Scarpine, M. Schubnell, I. Sevilla-Noarbe, R. C. Smith, M. Soares-Santos, F. Sobreira, M. E. C. Swanson, G. Tarle, J. Thaler, D. Thomas, A. R. Walker, and R. H. Wechsler. The DES Science Verification Weak Lensing Shear Catalogs. *ArXiv e-prints*, July 2015.

A. Kannawadi, C. A. Shapiro, R. Mandelbaum, C. M. Hirata, J. W. Kruk, and J. D. Rhodes. The Impact of Interpixel Capacitance on WFIRST PSFs. *ArXiv e-prints*, December 2015.

M. Kilbinger. Cosmology with cosmic shear observations: a review. *Reports on Progress in Physics*, 78(8):086901, July 2015. doi: 10.1088/0034-4885/78/8/086901.

K. Kuijken, C. Heymans, H. Hildebrandt, R. Nakajima, T. Erben, J. T. A. de Jong, M. Viola, A. Choi, H. Hoekstra, L. Miller, E. van Uitert, A. Amon, C. Blake, M. Brouwer, A. Buddendiek, I. F. Conti, M. Eriksen, A. Grado, J. Harnois-Déraps, E. Helmich, R. Herbonnet, N. Irisarri, T. Kitching, D. Klaes, F. La Barbera, N. Napolitano, M. Radovich, P. Schneider, C. Sifón, G. Sikkema, P. Simon, A. Tudorica, E. Valentijn, G. Verdoes Kleijn, and L. van Waerbeke. Gravitational lensing analysis of the Kilo-Degree Survey. *MNRAS*, 454:3500–3532, December 2015. doi: 10.1093/mnras/stv2140.

T. R. Lauer. The Photometry of Undersampled Point-Spread Functions. *PASP*, 111:1434–1443, November 1999a. doi: 10.1086/316460.

T. R. Lauer. Combining Undersampled Dithered Images. *PASP*, 111:227–237, February 1999b. doi: 10.1086/316319.

- R. Laureijs, J. Amiaux, S. Arduini, J. . Auguères, J. Brinchmann, R. Cole, M. Cropper, C. Dabin, L. Duvet, A. Ealet, and et al. Euclid Definition Study Report. *ArXiv e-prints*, October 2011.
- R. Mandelbaum. Instrumental systematics and weak gravitational lensing. *Journal of Instrumentation*, 10(05):C05017, 2015. URL <http://stacks.iop.org/1748-0221/10/i=05/a=C05017>.
- R. Mandelbaum, B. Rowe, R. Armstrong, D. Bard, E. Bertin, J. Bosch, D. Boutigny, F. Courbin, W. A. Dawson, A. Donnarumma, I. Fenech Conti, R. Gavazzi, M. Gentile, M. S. S. Gill, D. W. Hogg, E. M. Huff, M. J. Jee, T. Kacprzak, M. Kilbinger, T. Kuntzer, D. Lang, W. Luo, M. C. March, P. J. Marshall, J. E. Meyers, L. Miller, H. Miyatake, R. Nakajima, F. M. Ngolé Mboula, G. Nurbaeva, Y. Okura, S. Paulin-Henriksson, J. Rhodes, M. D. Schneider, H. Shan, E. S. Sheldon, M. Simet, J.-L. Starck, F.ureau, M. Tewes, K. Zarb Adami, J. Zhang, and J. Zuntz. GREAT3 results - I. Systematic errors in shear estimation and the impact of real galaxy morphology. *MNRAS*, 450:2963–3007, July 2015. doi: 10.1093/mnras/stv781.
- R. J. Marks. *Handbook of Fourier Analysis and Its Applications*. Oxford University Press, 1 edition, 2009.
- R. Massey, H. Hoekstra, T. Kitching, J. Rhodes, M. Cropper, J. Amiaux, D. Harvey, Y. Mellier, M. Meneghetti, L. Miller, S. Paulin-Henriksson, S. Pires, R. Scaramella, and T. Schrabback. Origins of weak lensing systematics, and requirements on future instrumentation (or knowledge of instrumentation). *MNRAS*, 429:661–678, February 2013. doi: 10.1093/mnras/sts371.
- M. J. McCaughrean. *The astronomical application of infrared array detectors*. PhD thesis, Edinburgh Univ. (Scotland)., 1987.
- P. McCullough. Inter-pixel capacitance: prospects for deconvolution. Technical report, August 2008.
- J E Meyers and P R Burchat. Impact of chromatic effects on galaxy shape measurements. *Journal of Instrumentation*, 9(03):C03037, 2014. URL <http://stacks.iop.org/1748-0221/9/i=03/a=C03037>.
- S. Miyazaki, Y. Komiyama, H. Nakaya, Y. Kamata, Y. Doi, T. Hamana, H. Karoji, H. Furusawa, S. Kawanomoto, T. Morokuma, Y. Ishizuka, K. Nariai, Y. Tanaka, F. Uraguchi, Y. Utsumi, Y. Obuchi, Y. Okura, M. Oguri, T. Takata, D. Tomono, T. Kurakami, K. Namikawa, T. Usuda, H. Yamanoi, T. Terai, H. Uekiyo, Y. Yamada, M. Koike, H. Aihara, Y. Fujimori, S. Mineo, H. Miyatake, N. Yasuda, J. Nishizawa, T. Saito, M. Tanaka, T. Uchida, N. Katayama, S.-Y. Wang, H.-Y. Chen, R. Lupton, C. Loomis, S. Bickerton, P. Price, J. Gunn, H. Suzuki, Y. Miyazaki, M. Muramatsu, K. Yamamoto, M. Endo, Y. Ezaki, N. Itoh, Y. Miwa, H. Yokota, T. Matsuda, R. Ebinuma, and K. Takeshi. Hyper Suprime-Cam. In *Society of Photo-Optical Instrumentation Engineers (SPIE) Conference Series*, volume 8446

of *Society of Photo-Optical Instrumentation Engineers (SPIE) Conference Series*, page 0, September 2012. doi: 10.1117/12.926844.

R. J. Noll. Zernike polynomials and atmospheric turbulence. *Journal of the Optical Society of America (1917-1983)*, 66:207–211, March 1976.

Jeffrey Kruk David Vaughnn Qian Gong Joseph Howard Alden Jurling Len Seals Eric Mentzell Nerses Armani Gary Kuan Pasquale et al., David Content. Optical design of the wfirst-afta wide-field instrument. *Proc. SPIE 9293, International Optical Design Conference 2014*, 2014.

S. Paulin-Henriksson, A. Amara, L. Voigt, A. Refregier, and S. L. Bridle. Point spread function calibration requirements for dark energy from cosmic shear. *A&A*, 484:67–77, June 2008. doi: 10.1051/0004-6361:20079150.

S. Paulin-Henriksson, A. Refregier, and A. Amara. Optimal point spread function modeling for weak lensing: complexity and sparsity. *A&A*, 500:647–655, June 2009. doi: 10.1051/0004-6361/200811061.

A. A. Plazas, G. M. Bernstein, and E. S. Sheldon. On-Sky Measurements of the Transverse Electric Fields’ Effects in the Dark Energy Camera CCDs. *PASP*, 126:750–760, September 2014. doi: 10.1086/677682.

A. Réfrégier. Weak gravitational lensing by large-scale structure. *Annual Review of Astronomy and Astrophysics*, 41:645–668, 2003.

J. D. Rhodes, R. J. Massey, J. Albert, N. Collins, R. S. Ellis, C. Heymans, J. P. Gardner, J.-P. Kneib, A. Koekemoer, A. Leauthaud, Y. Mellier, A. Refregier, J. E. Taylor, and L. Van Waerbeke. The Stability of the Point-Spread Function of the Advanced Camera for Surveys on the Hubble Space Telescope and Implications for Weak Gravitational Lensing. *ApJS*, 172:203–218, September 2007. doi: 10.1086/516592.

B. Rowe, C. Hirata, and J. Rhodes. Optimal Linear Image Combination. *ApJ*, 741:46, November 2011. doi: 10.1088/0004-637X/741/1/46.

B. T. P. Rowe, M. Jarvis, R. Mandelbaum, G. M. Bernstein, J. Bosch, M. Simet, J. E. Meyers, T. Kacprzak, R. Nakajima, J. Zuntz, H. Miyatake, J. P. Dietrich, R. Armstrong, P. Melchior, and M. S. S. Gill. GALSIM: The modular galaxy image simulation toolkit. *Astronomy and Computing*, 10:121–150, April 2015. doi: 10.1016/j.ascom.2015.02.002.

M. D. Schneider, D. W. Hogg, P. J. Marshall, W. A. Dawson, J. Meyers, D. J. Bard, and D. Lang. Hierarchical Probabilistic Inference of Cosmic Shear. *ApJ*, 807:87, July 2015. doi: 10.1088/0004-637X/807/1/87.



- S. Seshadri, C. Shapiro, T. Goodsall, J. Fucik, C. Hirata, J. D. Rhodes, B. T. P. Rowe, and R. M. Smith. Initial Results from a Laboratory Emulation of Weak Gravitational Lensing Measurements. *PASP*, 125:1065–1086, September 2013. doi: 10.1086/673318.
- C. Shapiro, B. T. P. Rowe, T. Goodsall, C. Hirata, J. Fucik, J. Rhodes, S. Seshadri, and R. Smith. Weak Gravitational Lensing Systematics from Image Combination. *PASP*, 125:1496–1513, December 2013. doi: 10.1086/674415.
- R. M. Smith, M. Zavodny, G. Rahmer, and M. Bonati. A theory for image persistence in HgCdTe photodiodes. In *Society of Photo-Optical Instrumentation Engineers (SPIE) Conference Series*, volume 7021 of *Society of Photo-Optical Instrumentation Engineers (SPIE) Conference Series*, page 0, July 2008. doi: 10.1117/12.789372.
- D. Spergel, N. Gehrels, J. Breckinridge, M. Donahue, A. Dressler, B. S. Gaudi, T. Greene, O. Guyon, C. Hirata, J. Kalirai, N. J. Kasdin, W. Moos, S. Perlmutter, M. Postman, B. Rauscher, J. Rhodes, Y. Wang, D. Weinberg, J. Centrella, W. Traub, C. Baltay, J. Colbert, D. Bennett, A. Kiessling, B. Macintosh, J. Merten, M. Mortonson, M. Penny, E. Rozo, D. Savransky, K. Stapelfeldt, Y. Zu, C. Baker, E. Cheng, D. Content, J. Dooley, M. Foote, R. Goullioud, K. Grady, C. Jackson, J. Kruk, M. Levine, M. Melton, C. Peddie, J. Ruffa, and S. Shaklan. Wide-Field InfraRed Survey Telescope-Astrophysics Focused Telescope Assets WFIRST-AFTA Final Report. *ArXiv e-prints*, May 2013.
- D. Spergel, N. Gehrels, C. Baltay, D. Bennett, J. Breckinridge, M. Donahue, A. Dressler, B. S. Gaudi, T. Greene, O. Guyon, C. Hirata, J. Kalirai, N. J. Kasdin, B. Macintosh, W. Moos, S. Perlmutter, M. Postman, B. Rauscher, J. Rhodes, Y. Wang, D. Weinberg, D. Benford, M. Hudson, W.-S. Jeong, Y. Mellier, W. Traub, T. Yamada, P. Capak, J. Colbert, D. Masters, M. Penny, D. Savransky, D. Stern, N. Zimmerman, R. Barry, L. Bartusek, K. Carpenter, E. Cheng, D. Content, F. Dekens, R. Demers, K. Grady, C. Jackson, G. Kuan, J. Kruk, M. Melton, B. Nemati, B. Parvin, I. Poberezhskiy, C. Peddie, J. Ruffa, J. K. Wallace, A. Whipple, E. Wollack, and F. Zhao. Wide-Field InfrarRed Survey Telescope-Astrophysics Focused Telescope Assets WFIRST-AFTA 2015 Report. *ArXiv e-prints*, March 2015.
- C. W. Stubbs. Precision astronomy with imperfect fully depleted CCDs: an introduction and a suggested lexicon. *Journal of Instrumentation*, 9:C03032, March 2014. doi: 10.1088/1748-0221/9/03/C03032.